Light-absorption enhancement of black carbon in the Asian outflow inferred from airborne SP2 and in-situ measurements during KORUS-AQ

Chaeyoon Cho[a], Joshua P. Schwarz[b], Anne E. Perring[b], Kara D. Lamb[b,c], Yutaka Kondo[d], Jong-Uk Park[a], Do-Hyeon Park[a], Kyuseok Shim[a], Jin-Soo Park[e], Rokjin J. Park[a], Meehye Lee[f], Chang-Keun Song[g], and Sang-Woo Kim[a,*]

[a]School of Earth and Environmental Sciences, Seoul National University, Seoul 08826, Republic of Korea
[b]NOAA Earth System Research Laboratory (ESRL), Chemical Sciences Division, Boulder, Colorado 80305, USA
[c]Cooperative Institute for Research in the Environmental Sciences (CIRES), University of Colorado, Boulder, Colorado 80309, USA
[d]National Institute for Polar Research, Tachikawa, Tokyo 190-8518, Japan
[e]National Institute of Environmental Research, Incheon 22689, Republic of Korea
[f]Department of Earth and Environmental Sciences, Korea University, Seoul 02841, Republic of Korea
[g]School of Urban and Environmental Engineering, Ulsan National Institute of Science and Technology, Ulsan 44919, Republic of Korea

*_Correspondence to_: Sang-Woo Kim (sangwookim@snu.ac.kr)

Revision Submitted to "Science of the Total Environment"

January 21, 2020

Abstract

We investigated the changes in the size distribution, coating thickness, and mass absorption cross-section (MAC) of black carbon (BC) with aging and estimated the light absorption enhancement (E_{abs}) in the Asian outflow from airborne in-situ measurements during 2016 KORUS-AQ campaign. The BC number concentration decreased, but mass mean diameter increased with increasing altitude in the West Coast (WC) and Seoul Metropolitan Area (SMA), reflecting the contrast between freshly emitted BC-containing particles at the surface and more aged aerosol associated with aggregation during vertical mixing and transport. Contradistinctively, BC number and mass size distributions were relatively invariant with altitude over the Yellow Sea (YS) because sufficiently aged BC from eastern China were horizontally transported to all altitudes over the YS, and there are no significant sources at the surface. The averaged inferred MAC of refractory BC in three regions reflecting differences in their size distributions increased to 9.8±1.0 $m^2\ g^{-1}$ (YS), 9.3±0.9 $m^2\ g^{-1}$ (WC), and 8.2±0.9 $m^2\ g^{-1}$ (SMA) as BC coating thickness increased from 20 nm to 120 nm. The absorption coefficient of BC calculated from the coating thickness and MAC were highly correlated with the filter-based absorption measurements with the slope of 1.16 and R^2 of 0.96 at 550 nm, revealing that the thickly coated BC had a large MAC and absorption coefficient. The E_{abs} due to the inferred coatings was estimated as 1.0–1.6, which was about 30% lower than those from climate models and laboratory experiments, suggesting that the increase in the BC absorption by the coatings in the Asian outflow is not as large as calculated in the previous studies. Organics contributed to the largest E_{abs} accounting for 69% (YS), 61% (WC), and 64% (SMA). This implies that organics are largely responsible for the lensing effect of BC rather than sulfates in the Asian outflow.

Keywords: Black carbon; Absorption enhancement; Aging process; SP2; KORUS-AQ

1. Introduction

Atmospheric black carbon (BC) aerosols emitted from the combustion of carbon-containing fuels contribute significantly to both global and regional warming of the atmosphere because they strongly absorb solar radiation (Ramana et al. 2010; Chung et al., 2012b; Bond et al., 2013; Liu et al., 2015). Direct warming effect of BC ranges from +0.08 to +1.27 W m^{-2}, but the estimates have a large uncertainty of 90% associated mainly with emissions, and the complicated aging and removal process in the atmosphere (Bond et al., 2013; Wang et al., 2014; Gustafsson and Ramanathan, 2016). Either during or soon after being emitted, BC becomes coated or mixed with other non-BC components (such as sulfate, nitrate, and organic components) through coagulation and condensation as a part of the aging process (Oshima et al., 2009; Ma et al., 2020). This aging process of mixing and coating can continuously alter the physical and optical properties of BC, resulting in light-absorption enhancement (E_{abs}) through the so-called lensing effect (Liu et al., 2015; Wu et al., 2018).

For estimating E_{abs} of coated BC particles, numerous modeling studies and laboratory experiments have been conducted based on the Mie theory calculations and absorption observations coupled with BC measurements, and those studies have reported that the BC absorption is amplified by up to a factor of 3 during the aging process (Bond et al., 2006; Shiraiwa et al., 2010; Wang et al., 2014; Cappa et al., 2019). Therefore, most current climate models simply assume a constant enhancement factor of 1.5–2.0 for scaling E_{abs} (Jacobson, 2001; Jacobson, 2013; Wang et al., 2014; Zhang et al., 2018a). However, recent field observations report smaller E_{abs} of no greater than 1.1 at visible wavelengths, even when substantial coatings occur in the atmosphere (Chan et al., 2011; Cappa et al., 2012; Nakayama et al., 2014; Healy et al., 2015; Cappa et al., 2019;

Xie et al., 2019). These previous field studies suggest that the effect of coatings on BC absorption in the real world is small, less than typically reported by the models and the laboratory experiments, which requires further research.

Several-week aircraft observations performing near-continuous horizontal and vertical profiling over synoptic scales in targeted areas can provide in-depth examination of the photochemical transformation and aging process of BC with greater spatial coverage (Redemann et al., 2000; Magi et al., 2003; Wofsy et al., 2011). However, such airborne BC measurements have been performed mostly in Europe and North America (Shiraiwa et al., 2007; Cappa et al., 2012; McMeeking et al., 2014; Healy et al., 2015; Liu et al., 2015; Cappa et al., 2019) although the regional climatic implications of BC have been recognized in East Asia, which contains some of the largest anthropogenic BC sources in the world (Zhang et al., 2009). The Korean Peninsula located downwind of the East Asia continent is an appropriate region for observing the active aging process and E_{abs} of BC because fresh emissions from Korea can be contrast with aerosols from various emission sources in China that can mix and coat with BC during long-range transport (Park et al., 2020).

The NASA DC-8 aircraft-based single-particle soot photometer (SP2) measurements, conducted during KORea-US cooperative Air Quality field campaign (KORUS-AQ; NIER and NASA, 2017) from May to June in 2016, provided an opportunity to investigate the physical properties of BC induced by the aging process and related changes in their optical properties during transport over the Korean Peninsula.

In this study, we investigated the changes in the physical and optical properties of BC caused by the aging process and estimated E_{abs} of BC in the Asian outflow from the airborne SP2 observations collected during the KORUS-AQ campaign. In section 3.1, we

present an overview of the temporal and spatial distribution of aerosol optical properties and BC physical properties from in-situ aircraft measurements. To better understand the variations in the physical properties with the aging process according to the regional and local impacts of BC emissions, vertically resolved BC size distribution was analyzed in section 3.2. Based on the observed size distribution of BC particles, and light-scattering measurements used to infer internal mixtures with the BC (i.e., "coatings"), the changes in the mass absorption cross-section (MAC) of BC were simulated by the Mie core-shell model in section 3.3. We also discuss the absorption enhancement of BC over the Korean Peninsula and the major chemical compositions contributing to E_{abs} in sections 3.4 and 3.5, respectively.

2. Measurements and analysis

2.1 Airborne in-situ aerosol measurements

Comprehensive airborne in-situ measurements of aerosol physical, chemical, and optical properties used in this study were taken onboard the NASA DC-8 aircraft over the Korean Peninsula during the KORUS-AQ campaign (Al-Saadi et al., 2015; NIER and NASA, 2017; Lamb et al., 2018). Aerosol scattering coefficients (σ_{sp}) and aerosol absorption coefficients (σ_{ap}) were measured using a three-wavelength (450, 550, and 700 nm) nephelometer (model 3563, TSI Inc.) and a particle soot absorption photometer (PSAP; Radiance Research), respectively. The σ_{sp} and σ_{ap} measured at 550 nm were used to calculate the single scattering albedo (SSA).

This study focuses on the refractory BC (rBC) mass, size distributions, and the coating thickness in the accumulation-mode size range, measured using the U.S. National Oceanic and Atmospheric Administration (NOAA) SP2 (Droplet Measurement

Technologies; Schwarz et al., 2013; Lamb et al., 2018). In the SP2 technique, the mass of rBC in a single particle is determined from its laser-induced incandescence signal. This is linearly proportional to the rBC mass over most of the rBC mass in the accumulation mode size range (Schwarz et al., 2008). The sensitivity of the SP2 to single-particle rBC mass was calibrated using size-selected fullerene soot (Lot F12S011, Alfa Aesar Inc., Woodhill, MA) and using the mass-mobility relationship for this material from Gysel et al. (2011). The empirical relationship between mobility diameter and single particle rBC mass was previously determined for SP2 measurements of fullerene soot (Moteki and Kondo, 2010; Lamb et al., 2018). During the campaign period, mass calibrations with the differential mobility analyzer were performed six times and the average linear fit across all calibrations was used for processing data. The SP2's sampling flow rate was calibrated just before the campaign. Pre-flight and in-flight calibrations of the SP2 were made with polystyrene latex spheres to determine laser intensity for aerosol optical size measurements from the scattered light signals measured by two avalanche photodiodes (Gao et al., 2007). A temperature dependent correction was applied to the measured scattering signal to account for the laser power reduction at high temperatures, based on an observed correlation between the polystyrene latex sphere modal scattering signals and instrument temperature at the same laser current (Lamb et al., 2018). SP2 instrument response was stable within 5% for this accepted rBC reference material over the duration of the campaign (Baumgardner et al., 2012). The SP2 quantified particles containing 0.7–150 fg of rBC material (equivalent to core sizes of 90–500 nm volume equivalent diameter assuming a void-free density of 1.8 g cm^{-3}), which is independent of the presence or the amount of coexisting non-refractory material. Integration of rBC mass observed within sampled air was used to calculate the mass-concentration of the

rBC (M_{rBC}). The SP2 also provided optical sizing of individual rBC-containing particles with 4–6 fg rBC mass through the analysis of elastically scattered laser light prior to significant thermal perturbation by the laser (Gao et al., 2007). The early scattering signal allowed for the quantification of non-refractory material mixed with rBC, referred to here as coatings. The coating thickness was calculated as the difference between the optical diameter determined from the scattering signal and the mass-equivalent diameter of rBC determined from the incandescence signal. This coating thickness is that which would occur if the coating were uniformly distributed around the rBC (Sedlacek et al., 2012). The actual physical arrangement of the rBC and non-rBC component is not known, and a simple spherical core and shell approximation is assumed. The coating thickness of rBC was calculated from the measured optical size based on the Mie theory, which assumes a spherical core-shell morphology and both coating and rBC indices of refraction (Schwarz et al., 2008). Coating thickness was aggregated in 2-minute averages for use in this study. The configurations and operating mechanism of SP2 have been described in previous studies (Schwarz et al., 2006; Schwarz et al., 2008; Moteki et al., 2010). The detailed explanation of airborne SP2 measurements during the KORUS-AQ campaign is presented in Lamb et al. (2018).

The chemical components and mass information of non-refractory sub-micrometer particulate matter (NR-PM_1), including organic aerosol, sulfate, nitrate, and ammonium concentrations, were measured using an Aerodyne high-resolution time-of-flight aerosol mass spectrometer (HR-ToF-AMS), which vaporizes and ionizes targeted particles at 600 °C (DeCarlo et al., 2006). The data obtained from the HR-ToF-AMS were processed using the standard toolkit (SeQUential Igor data RetRiEval and PIKA; Jimenez et al.,

2003). The detailed data processing procedures used during the KORUS-AQ campaign are described in Nault et al. (2018).

2.2 Simulation of uncoated and coated BC absorption

We calculated the absorption properties of uncoated and coated BC particles at multiple incident wavelengths between 250 and 900 nm in steps of 50 nm, based on the Mie core-shell model of Toon and Ackerman (1981). The size distribution and coating thickness from SP2 measurements were constrained as input data for core and shell diameters of the particles, respectively. It is assumed that all particles in the atmosphere including both BC (i.e., core of particles) and non-BC particles (i.e., shell of particles) have homogenous spherical morphology. The observed BC core diameter of 100–500 nm with 17 bins was extrapolated to 10–1000 nm by the lognormal distribution fitting assuming conversion from the measured masses with void-free density 1.8 g cm^{-3}. In this study, the uncoated BC means only considering their core size immediately after emitted without coating. The absorption cross-section of a single uncoated BC particle was calculated using the refractive index of BC and optical sizing of individual rBC particle observed from SP2. The BC having a shell as much as the coating thickness observed from SP2 was defined as coated BC. The absorption cross-section of coated BC was calculated using the refractive index of shell and the inferred coating thickness from SP2. The refractive indices of BC and shell were set to be the variable wavelength-dependent values used in global models, including the software package of Optical Properties of Aerosols and Clouds (OPAC; Hess et al., 1998). For example, $1.75–0.44i$ and $1.44–0i$ were used for the refractive index of the BC core and shell at 550 nm, respectively. The absorption cross-section corresponding to each size of core and shell

198 (i.e., uncoated and coated BC) was obtained at wavelengths from 250 to 900 nm, and
199 converted to their MAC by applying the number and mass concentrations, and void-free
200 density of 1.8 g cm^{-3} (Gao et al., 2007; Moteki et al., 2010).
201

202 # 3. Results and discussion

203 ## 3.1 Overview of DC-8 aerosol measurements

204 The overall characteristics of aerosol optical properties (σ_{sp}, σ_{ap}, SSA) and rBC
205 physical properties (M_{rBC}, coating thickness) from the DC-8 aircraft measurements in
206 the East Asian outflow showed distinct temporal and vertical variations (Table S1 and
207 Figure 1). The periods during the KORUS-AQ campaign were divided into four different
208 meteorological synoptic patterns (Figure S1, Lamb et al., 2018, Peterson et al., 2019):
209 dynamic period (May 2–13), stagnant period (May 17–22), transport period (May 25–
210 31), and blocking period (June 2–10). During the dynamic period, strong wind field and
211 pressure gradient led to the lowest values of σ_{sp} (30±22 Mm^{-1}), σ_{ap} (2.4±2.0 Mm^{-1}), SSA
212 (0.92±0.03), M_{rBC} (0.17±0.14 μg m^{-3}), and rBC coating thickness (47±10 nm). These
213 parameters continuously decreased with the increasing altitude but showed relatively
214 small vertical variations compared to other periods. Starting after the stagnant period,
215 the parameter values began to increase and maintained their high values until the
216 blocking period.

217 The σ_{sp} value averaged over the stagnant period was 74±55 Mm^{-1} and distinctly
218 increased to 114±92 Mm^{-1} in the transport period. The high value of σ_{sp} was maintained
219 during the blocking period at the level of 107±77 Mm^{-1}. Compared to σ_{sp}, σ_{ap} and M_{rBC}
220 did not show significant changes before and after the transport period even though the
221 maximum average values of σ_{ap} (6.4±4.9 Mm^{-1}) and M_{rBC} (0.42±0.33 μg m^{-3}) were

observed during the transport period. The large increase in σ_{sp} compared to σ_{ap} and M_{rBC} suggests that light-scattering aerosols were dominantly increased, as indicated by the continuously increased SSA from stagnant (0.93±0.02) to blocking (0.95±0.02) periods. On the contrary, the rBC coating thickness was the highest in the stagnant period (72±19 nm), followed by the transport (63±11 nm) and blocking (62±10 nm) periods, suggesting that complex physicochemical transformation in the atmosphere affects the coating thickness of BC.

Representing an important light absorbing property of aerosols containing aged BC, σ_{ap} averaged from the surface to the 2 km altitude showed distinct spatial distribution depending on the sub-regions affected by the pollutants emitted from specific sources within the region and/or transported over long range (Figure S2). For example, long-range transport of air pollutants heavily impacts the concentrations over the Yellow Sea (YS), while local emissions from power plants, petrochemical plants, and other manufacturing industries predominantly affect the West Coast (WC) of the Korean Peninsula (Oak et al., 2019). Local anthropogenic emissions from commercial, industrial, and residential sources and vehicle emissions are dominant in the Seoul Metropolitan Area (SMA; Kim et al., 2018). These sources co-emit both BC and carbon monoxide (CO) during incomplete combustion, but BC is more rapidly removed than CO; therefore, the higher ratio of BC to CO mass concentrations indicates the effect of fresher emissions (Spackman et al., 2008; Kanaya et al., 2016; Choi et al., 2020). Figure 2 shows the relationship between BC and CO mass concentrations with slopes observed in three selected regions for each period during the KORUS-AQ campaign. For all periods, the highest BC/CO slope of 3.3–5.3 was observed in the SMA due to the influence of dominant fresher local emissions. The BC/CO slopes in the WC during the dynamic and

stagnant periods were almost the same as those in the SMA, which also reflects the impact of freshly emitted BC and the lower impact of the long-range transport of aerosols. In the YS, the BC/CO slope was the lowest (2.1–2.6) due to the larger impact of transported aerosols and the lowest impact of local sources. In addition, BC aerosols transported to the YS were likely removed efficiently through a wet scavenging process while crossing the ocean. Similarly, Choi et al. (2020) diagnosed the ΔBC/ΔCO ratios from long-term, best effort observations at four sites in East Asia (Baengnyeong and Gosan in Korea; Fukuoka and Noto in Japan) and reported that the ratios from four sites converged into a narrow range (6.2–7.9 ng m^{-3} ppb^{-1}). However, the ΔBC/ΔCO ratios at Baengnyeong and Gosan in Korea were higher than that at Fukuoka and Noto in Japan because the Baengnyeong and Gosan were mainly influenced by the southwestern region of South Korea, including the SMA.

3.2 Changes in size distribution of rBC with aging process

Because freshly emitted BC particles in bare conditions are aggregated into small carbon spherules during vertical and/or horizontal transportation, the number and mass size distribution of rBC can reveal information on the aging process of BC aerosols. Figure 3 shows the altitude-resolved number and mass size distributions of rBC from the surface to 2 km with 500 m intervals in three regions (YS, WC, and SMA). The rBC number concentrations near the surface in the WC (6100±1174 # cm^{-3}) and SMA (6809±1452 # cm^{-3}) were approximately 2.5 times higher than that in the YS (2359±781 # cm^{-3}) owing to the direct impact of the large amount of BC emitted from local sources. However, the rBC number concentration continuously decreased with the increasing altitude in the WC and SMA whereas that in the YS did not change significantly, resulting

in similar rBC number concentrations ranging from 1800 to 2000 cm^{-3} at the altitudes above 1 km (Figure 3a).

The mass size distribution and mass median diameter of rBC (MMD_{rBC}) were more directly related to both the emission sources and air parcel history (Moteki et al., 2012; Ohata et al., 2016; Lamb et al., 2018). According to the previous studies, the distributions of rBC particle sizes in urban and background regions are significantly different (Wentzel et al., 2003; Andreae and Gelencsér, 2006). In general, MMD_{rBC} in urban regions is below 200 nm, and that in background regions is approximately 200 nm (Schwarz et al., 2008; McMeeking et al., 2010; Liu et al., 2020). The MMD_{rBC} observed in the YS was in the range of 202–209 nm, indicating the predominance of the transported BC aerosols. Several studies from the KORUS-AQ campaign also reported that heavy loadings of aerosols emitted in eastern and northeastern China, wind-blown mineral dust particles, and smoke from fires in Siberia were frequently transported to the YS (Choi et al., 2019; Park et al., 2020). As the transported aerosols sufficiently aged and horizontally transported to all altitudes over the YS, the MMD_{rBC} showed no significant changes with altitudes. The MMD_{rBC} in the SMA was from 163 to 188 nm, corresponding to that reported for locally emitted pollutants from vehicles, high population density areas, and industry (Figure 3b). The steady increase in MMD_{rBC} and decrease in $dM/dlogD_{rBC}$ with altitude indicated prominent BC spherule formation through the coagulation of BC aggerates during vertical mixing within the boundary layer in the SMA. Compared to the YS, long-range transport of aerosols from China to the SMA takes place very rarely in the upper layers. MMD_{rBC} in the WC demonstrated two distinctive ranges depending on the altitude. At low altitudes below 1 km, the smaller MMD_{rBC} of 179–189 nm was observed, indicating the influence of the petrochemical

complexes in the WC. The larger MMD_{rBC} of 205–210 nm was observed at the altitudes above 1 km, similar to that observed in the YS. The long-range transport of aerosols from China and Siberia to the YS has affected the WC as well. Additionally, the smaller particles suspended at low altitudes aggregated and grew during transport in the vertical direction, leading to the increased MMD_{rBC} in the upper layer.

3.3 Changes in mass absorption cross-section (MAC) of rBC with coatings

In all three regions, the calculated MAC of uncoated rBC ($MAC_{rBC}^{Uncoated}$) demonstrated the intrinsic property of BC that does not rely on synoptic meteorological patterns and altitudes with a relatively constant value of 6.3±0.5 $m^2 g^{-1}$ (YS), 6.1±0.4 $m^2 g^{-1}$ (WC), and 5.6±0.5 $m^2 g^{-1}$ (SMA) at 550 nm. This is a reflection of the weak dependence of $MAC_{rBC}^{Uncoated}$ on the size distribution of rBC. The $MAC_{rBC}^{Uncoated}$ values at 550 nm in three regions were approximately 15–25% lower than that expected for combusted fresh BC (7.5±1.2 $m^2 g^{-1}$ at 550 nm; Bond and Bergstrom, 2006), which has been generally used in many global models, but similar to MAC_{BC}, which had no mixing effect with other substances in Gosan, Korea (5.1±0.9 $m^2 g^{-1}$ at 520 nm in Chung et al., 2012a; 6.4±1.5 $m^2 g^{-1}$ at 565 nm in Cho et al., 2019). In addition to several parameters (i.e., size distribution, core size, and mass concentration of BC), this discrepancy between the model and observations shows that the assumption of conventional modeling for pure BC can overestimate the radiative forcing in the East Asian outflow.

The $MAC_{rBC}^{Uncoated}$ has changed by aging process of BC in the ambient atmosphere. Especially, the evolution of BC coating thickness accompanied by restructuring of the aggregates to spheres significantly affects the absorption capability of BC by changing their size and refractive indices (Ma et al., 2020). The coating thickness measured from

SP2 onboard the DC-8 aircraft was in the wide range of 20–120 nm during the KORUS-AQ campaign. To assess the impact of the coating thickness on the absorption properties of BC, the changes in the σ_{ap} and MAC of rBC with the coatings were investigated. Figures 4 and 5 show the observed σ_{ap} and MAC of coated rBC (MAC_{rBC}^{Coated}), separated by the region, meteorological condition, and altitude. The σ_{ap} and MAC_{rBC}^{Coated} show increases with the rBC coating thickness; thinly (thickly) coated BC had a small (large) σ_{ap} and MAC. It should be noted that σ_{ap} observed from PSAP and calculated by SP2 observation and Mie core-shell model were highly correlated with the slope of 1.16 and R^2 of 0.96 at 550 nm (Figure S3). In the three regions, BC particles exhibited large variations in MAC_{rBC}^{Coated} from 6 to 12 $m^2\ g^{-1}$ at 550 nm, with the average MAC_{rBC}^{Coated} of 9.8±1.0 $m^2\ g^{-1}$ (YS), 9.3±0.9 $m^2\ g^{-1}$ (WC), and 8.2±0.9 $m^2\ g^{-1}$ (SMA). These values were within the range of 8–12 $m^2\ g^{-1}$ in the surface measurements taken in the polluted urban environments in East and South Asia (Kondo et al., 2009; Ram and Sarin, 2009; Yang et al., 2009; Cheng et al., 2011; Cui et al., 2016) and airborne measurements taken in major source regions in the United Kingdom (McMeeking et al., 2011).

As illustrated in Figures 4 and 5, the variations in σ_{ap} and MAC_{rBC}^{Coated} with rBC coating thickness should be interpreted in conjunction with the observed meteorological periods and altitudes in each region. The average coating thickness was similar in all regions (YS: 63±19 nm, WC: 65±16 nm, SMA: 57±16 nm), but their distribution was different between the regions affected by the long-range transport versus local emissions of aerosols. In the YS, the distribution of rBC coating thickness exhibited two dominant modes, maxima between 30–60 nm (a smaller mode) and 70–90 nm (a larger mode). The overall slope between rBC coating thickness and MAC_{rBC}^{Coated} was the largest during the transport period (0.057) (Table S2), indicating

that the MAC_{rBC}^{Coated} increased most significantly with the increasing coating thickness by transported non-BC aerosols. It also led to the distinct increase of σ_{ap}. This positive relationship was more evident at the altitudes below 1.5 km than at high altitudes. Below 1.5 km in the YS, the SO_4^{2-} concentration was twice as high as those in the other regions (Figures S4 and S5). Previous studies have revealed that sulfate is a primary driver of enhanced BC absorption among aged BC coating materials (Shiraiwa et al., 2007; Kondo et al., 2011; Zhang et al., 2017). Lim et al. (2018) reported the significance of sulfate-dominated and increased ambient relative humidity (RH) environment in enhancing MAC_{BC} in East Asia. Jordan et al. (2020) also observed that cloudy humid conditions fostered rapid heterogeneous secondary inorganic aerosol production from local and transported emissions, likely driven by a positive feedback mechanism where water uptake by aerosols increased gas-to-particle partitioning that increased water uptake during KORUS-AQ campaign. Therefore, the abundant sulfate at lower altitudes in the YS may have formed thick coatings by condensation with sufficient water vapor evaporated from the surrounding sea, resulting in enhanced σ_{ap} and MAC_{rBC}^{Coated}. On the contrary, the smaller mode with thinner coatings and a slight increase in σ_{ap} and MAC_{rBC}^{Coated} were mainly observed in the upper layer (>2 km). This is because BC particles with sufficiently increased coating thickness act as cloud condensation nuclei or are quickly removed by wet/dry deposition in the upper layer (Taylor et al., 2014).

The WC and SMA had a similar unimodal distribution with a dominant coating thickness mode between 20–90 nm. The coating thickness in this range generated a strong linear relationship with MAC_{rBC}^{Coated}, showing the best relationship with slopes of 0.065 (WC) and 0.049 (SMA) in the blocking period (Table S2). In addition, the relationship between the coating thickness and MAC_{rBC}^{Coated} according to the altitude

366 was less pronounced than that of the YS. As evident in Figure S1, winds were weak and
367 the air mass containing aerosols was trapped over the Korean Peninsula due to the
368 persistent high-pressure system located centered in East Asia in the blocking period.
369 These stable atmospheric conditions provided favorable conditions to accumulate
370 organics, SO_4^{2-}, and NO_3^- emitted from power plants and industrial sectors located in the
371 western part of the Korean Peninsula (Peterson et al. 2019; Lamb et al., 2018; Park et al.,
372 2020), likely contributing to various coating thickness values. BC coated with the
373 observed chemical species caused large MAC_{rBC}^{Coated} variations in the range of 6–12 m^2
374 g^{-1}, wherein thinly (thickly) coated BC exhibited small (large) MAC. Because the effects
375 of abundant organic and inorganic species on coated BC were rather complex, it is
376 difficult to observe a direct relationship between coating thickness and MAC of BC.
377 Theoretical modeling and laboratory experiments demonstrated that the increase in BC
378 coating resulted from a combination of different sources, type of coating materials, and
379 photochemical aging processes (Liu et al., 2015). Peng et al. (2016) revealed
380 photochemically produced secondary organic aerosols (SOA) as the coating materials
381 from the particle composition measurements using an Aerosol Mass Spectrometer
382 (AMS).

383 The influence of SOA on BC coating was evident in the stagnant period in all three
384 regions. The concentration of organics showed a notable increase in the stagnant period
385 compared to SO_4^{2-} and NO_3^- (Figure S4). Previous studies on the KORUS-AQ campaign
386 reported that a substantial amount of organics were emitted from local sources in the
387 Korean Peninsula and transported by aged smoke from fires in Siberia in this period,
388 while transport from China and Mongolia were blocked (Peterson et al., 2019; Lamb et
389 al., 2018; Park et al., 2020). Kim et al. (2018) reported that the accumulation of organic

aerosols during the stagnant period is related to an increase in the concentrations of volatile organic compounds (VOCs) coupled with the high concentration of O_x (O_3 + NO_2), strong solar radiation, and stagnant conditions, which together promote intensive formation of SOA. This was further explored by Jordan et al. (2020) in an analysis of stagnant period during KORUS-AQ campaign that clear and dry conditions with limited transport promoted photochemical production of SOA from locally emitted precursors. Thus, increased MAC_{rBC}^{Coated} with the thickest coating of 90–120 nm during the stagnant period can be explained by the combined effect of primary organic aerosol (POA) and SOA, highlighting the significance of photochemical production of the BC coating materials.

3.4 Enhancement of rBC absorption (E_{abs})

Overall E_{abs} at 550 nm, calculated as the ratio of MAC_{rBC}^{Coated} to $MAC_{rBC}^{Uncoated}$, during the KORUS-AQ campaign ranged from 1.0 to 2.0 (Figure 6). For the rBC diameter of 100–550 nm, E_{abs} increased as the larger amount of substances coated on the smaller diameter rBC. In other words, the ratio between the coated and uncoated rBC radius (R_p/R_{rBC}; R_p = R_{rBC} + rBC coating thickness) determined the magnitude of E_{abs}. The rBC light absorption at 550 nm increased by a factor of 2 when the R_p/R_{rBC} ratio was the maximum value of 2.8, although it mostly increased by a factor of 1.0–1.6. Therefore, the increase in light absorption of BC by coatings over the Korean Peninsula was not as large as that reported in previous modeling studies and laboratory experiments.

During the dynamic period, the air mass containing BC and non-BC aerosols rapidly flowed into the upper layer over the Korean Peninsula, resulting in a similar coating thickness to that observed in China, but E_{abs} in three regions in Korea was 25% lower

than that estimated in China. After the dynamic period, as the air mass became stagnant over the Korean Peninsula, the coating thickness gradually increased, showing an average thickness of 90 nm under stable atmospheric conditions in the YS and WC. This range of coating thickness in the stagnant period was similar to that simulated by Zhang et al. (2017), but E_{abs} was 30% lower. As evident in Figure 6, there was no significant difference in the observed rBC diameter depending on the meteorological conditions and regions, but the coating thickness varied by a factor of two, resulting in large E_{abs} variations ranging from 1.34 to 1.68. E_{abs} in the YS was 5% higher than that in the SMA for an identical period due to the combined effect of abundant aerosols from local and regional emissions, and humid atmospheric conditions owing to the surrounding ocean. Park et al. (2020) reported that the hygroscopicity parameter over the YS of 0.36 was three times higher than that in the SMA of 0.11 during the KORUS-AQ campaign, showing the strong dependence of BC absorption on relative humidity.

For an identical R_p/R_{rBC} ratio, E_{abs} in this study was about 30% lower than those in climate models and laboratory experiments. For example, at R_p/R_{rBC}=1.8, average E_{abs} in this study and from the climate model was 1.45 and 1.8 (Zhang et al., 2017), respectively. At R_p/R_{rBC}=1.5, average E_{abs} in this study was 1.15, whereas that from laboratory experiments was 1.62 (Shiraiwa et al., 2010). This comparison reveals that the absorption enhancement of BC in the real atmosphere is not as large as simulated in the model, showing consistency with the previous studies reporting smaller absorption enhancement in field observations (Cappa et al., 2012; Nakayama et al., 2014; Healy et al., 2015; Cappa et al., 2019). However, E_{abs} in this study was approximately 10% lower than those observed in polluted urban environments in Xianghe (1.42; Zhang et al., 2016) and Beijing (1.4; Peng et al., 2016). This is because that the high concentration of non-

BC components emitted in the source regions quickly coated the BC aerosols within 2–5 hours, contributing to an increase in the coating thickness and E_{abs} in polluted urban areas. On the contrary, a less active coagulation process and partial evaporation of the coating materials used for BC during the long-range transport (Popovicheva et al., 2011; Leung et al., 2017; Lim et al., 2018; Cho et al., 2019) can explain the lower coating thickness and E_{abs} downwind of the BC source regions. Although E_{abs} over the Korean Peninsula was lower than in polluted regions, it was still higher than in less polluted sites in North America and Europe (Chan et al., 2011; Healy et al., 2015; Peng et al., 2016), suggesting that BC with coatings in East Asia can significantly contribute to the positive radiative forcing of carbonaceous aerosols.

3.5 Contribution of aerosol chemical composition to E_{abs}

The variations in the total coating thickness of BC are closely related to the concentration of each chemical species in bulk fine mode aerosol, which are co-emitted with BC, long-range transported, and formed by the photochemical processes in the atmosphere (Peng et al., 2016). To estimate which chemical species has the most significant effect on E_{abs} as the coating material, the relative contribution of each chemical fraction to E_{abs} was evaluated via multivariate linear regression analysis (Zhang et al., 2018b). The multivariate linear regression analysis allowing for elucidating the influence of each chemical species on E_{abs} was applied following the equation (Eq. 1):

$$E_{abs} = a_0 + a_1[\text{Organic-to-BC}] + a_2[\text{Sulfate-to-BC}] + a_3[\text{Nitrate-to-BC}] + a_4[\text{Ammonium-to-BC}] \quad (1)$$

where, a_i is regression coefficient and bracket ([ ]) represents averaged ratio of the chemical fraction to BC. To reduce the influence of outliers, data points both lower than 5th and upper than the 95th percentiles were excluded. This analysis was carried out based on the assumption that only organics, SO_4^{2-}, NO_3^-, and NH_4^+ contribute to E_{abs}. Figure 7 shows the contribution of each chemical composition to E_{abs} in each meteorological period and region. The variations in the contribution of the chemical composition were consistent with those in the relative chemical fractions in total non-refractory submicron aerosol concentrations (Figure S6).

During the stagnant period, when E_{abs} was the largest, the major contributor was the organics accounting for 69% (YS), 61% (WC), and 64% (SMA). Sulfate, considered a major coating material in previous studies, only increased during the transport period, accounting for 50% (YS and WC) and 38% (SMA). This result suggests that organics are likely responsible for the lensing effect of BC rather than sulfates. Although little is understood about the coating mechanism and quantitative effect of organics and sulfates on E_{abs}, the combined influence of both POA and SOA would have contributed to the largest E_{abs} values. It is challenging to predict and attribute the specific organic compounds and sources that lead to the highest contribution to E_{abs}. However, Zhang et al. (2018b) reported that more oxidized oxygenated organic aerosols (OOAs) had a much higher impact on light absorption than less oxidized OOA and sulfates, and Liu et al. (2015) found that the more OOAs were associated with the long-range transport and aging of particles. In contrast, Nault et al. (2018) and Jordan et al. (2020) reported that production of SOA from locally emitted precursors was the major source of organics in the SMA.

During the dynamic period when E_{abs} was the smallest, organics and SO_4^{2-} were still major contributors to E_{abs}, but the contribution of NH_4^+ was noticeably high. NH_4^+, which is mainly emitted from on-road vehicles, neutralizer use in industry, and agricultural biomass burning, plays an important role in the rapid formation of $(NH_4)_2SO_4$ due to the interaction of ions, and it is likely to prevent SO_4^{2-} from being coating materials (Si et al., 2017). Thus, relatively smaller E_{abs} is attributable to the increased contribution of NH_4^+. The higher contribution of NH_4^+ in the YS offers the possibility that NH_4^+ is emitted from the plankton activity in the ocean (Klawonn et al., 2019).

4. Summary

Airborne in-situ measurements of physical, chemical, and optical properties of ambient aerosols carried out in the Asian outflow during the KORUS-AQ campaign in 2016 enabled us to estimate the changes in the size distribution and MAC of BC depending on the aging process, and the light absorption enhancement.

The continuously decreased number concentration and increased MMD_{rBC} with the increasing altitude in the WC and SMA indicated that freshly emitted small-sized rBC particles near the surface were aggregated by coagulating with each other during vertical mixing within the boundary layer. There was no significant changes in the rBC number and mass size distribution with altitude over the YS because sufficiently aged BC aerosols were transported horizontally into all altitudes over the YS from eastern China.

The evolution of BC coating thickness by the aging process was closely related to the changes in the MAC of rBC. The average $MAC_{rBC}^{Uncoated}$ of 6.3±0.5 $m^2\ g^{-1}$ (YS), 6.1±0.4 $m^2\ g^{-1}$ (WC), and 5.6±0.5 $m^2\ g^{-1}$ (SMA) at 550 nm increased to 9.8±1.0 $m^2\ g^{-1}$ (YS), 9.3±0.9

510 $m^2\ g^{-1}$ (WC), and 8.2±0.9 $m^2\ g^{-1}$ (SMA) as BC coating thickness increased from 20 nm to
511 120 nm. MAC_{rBC}^{Coated} by rBC coating thickness was in conjunction with observed
512 meteorological periods and altitudes in each region. In the YS, MAC_{rBC}^{Coated} increased
513 most significantly at altitudes below 1.5 km during the transport period because
514 abundant sulfate was transported and formed thick coatings by condensation with
515 sufficient water vapor evaporated from the surrounding sea. In the WC and SMA, the
516 coating thickness and MAC_{rBC}^{Coated} showed a strong relationship in the blocking period.
517 The stable atmospheric conditions in the blocking period provided favorable conditions
518 to accumulate organic, SO_4^{2-}, and NO_3^- emitted from local sources, resulting in various
519 coating thickness and MAC_{rBC}^{Coated} values, wherein thinly (thickly) coated BC exhibited
520 small (large) MAC. In all three regions, the highest MAC_{rBC}^{Coated} and coating thickness of
521 more than 90 nm was observed during the stagnant period due to the combined effect of
522 POA and SOA, highlighting the significance of photochemical production of the BC
523 coating materials.

524 The E_{abs} due to the inferred coatings was estimated as 1.0–1.6 at 550 nm. The largest
525 E_{abs} value was contributed by organics accounting for 69% (YS), 61% (WC), and 64%
526 (SMA). Sulfate only increased during the transport period (50% in YS and WC, 38% in
527 SMA), suggesting that organics are likely responsible for the lensing effect of BC rather
528 than sulfates in the Asian outflow.

529 Our airborne observation-based estimates revealed that the enhancement in light
530 absorption of BC by coatings over the Korean Peninsula was not as large as that
531 reported in previous studies based on the model results and laboratory experiments.
532 However, E_{abs} over the Korean Peninsula was still higher than in less polluted sites in
533 North America and Europe, suggesting that BC with coatings in East Asia significantly

534 contributes to large positive radiative forcing of carbonaceous aerosols. Further
535 investigation of realistic BC morphology and coating structures in the ambient air is
536 required to improve the estimates of BC radiative effects in climate models.
537

CRediT authorship contribution statement

Chaeyoon Cho: Formal analysis, Visualization, Writing - original draft & editing. **Joshua P. Schwarz**: Investigation, Resources, Validation, Data Curation. **Anne E. Perring**: Investigation, Resources, Validation, Data Curation. **Kara D. Lamb**: Investigation, Resources, Validation, Data Curation. **Yutaka Kondo**: Investigation, Resources, Validation, Data Curation. **Jong-Uk Park**: Formal analysis. **Do-Hyeon Park**: Formal analysis. **Kyuseok Shim**: Formal analysis. **Jin-Soo Park**: Investigation, Resources. **Rokjin J. Park**: Methodology, Validation, Writing - review & editing. **Meehye Lee**: Methodology, Validation, Writing - review & editing. **Chang-Keun Song**: Methodology, Validation, Writing - review & editing. **Sang-Woo Kim**: Conceptualization, Investigation, Writing - original draft, review & editing, Supervision.

Declaration of competing interest

None.

Acknowledgments

The authors are grateful to the NASA DC-8 pilots and crew, and to all members of the KORUS-AQ science team for their contributions during the field campaign and the agencies operating the surface networks. This research was supported by Basic Science Research Program through the National Research Foundation of Korea (NRF) funded by the Ministry of Education (2020R1A6A3A01097230), the Korea Meteorological Administration Research and Development Program under Grant KMI2018-01111, and by the FRIEND (Fine Particle Research Initiative in East Asia Considering National Differences) Project through the National Research Foundation of Korea (NRF) funded by the Ministry of Science and ICT (Grant No.: 2020M3G1A1114615). The NOAA SP2 data were obtained and analyzed with the support of the NASA Radiation Sciences

564 Program, the NASA Upper Atmosphere Research Program, the NASA Tropospheric
565 Chemistry Program, and the NOAA Atmospheric Composition and Climate Program.
566

References

Al-Saadi, J., Carmichael, G., Crawford, J., Emmons, L., Song, C.-K., Chang, L.-S., Lee, G., Kim, J., Park, R.J., 2015. NASA contributions to KORUS-AQ: An international cooperative air quality field study in Korea.

Andreae, M.O., Gelencsér, A., 2006. Black carbon or brown carbon? The nature of light-absorbing carbonaceous aerosols. Atmos. Chem. Phys. 6, 3131–3148.

Baumgardner, D., and Co-authors, 2012. Soot reference materials for instrument calibration and intercomparisons: A workshop summary with recommendations, Atmos. Meas. Tech. 5, 1869–1887.

Bond, T.C., Bergstrom, R.W., 2006. Light absorption by carbonaceous particles: An investigative review. Aerosol Sci. Technol. 40, 27–67.

Bond, T.C., Doherty, S.J., Fahey, D.W., Forster, P.M., Berntsen, T., DeAngelo, B.J., Flanner, M.G., Ghan, S., Kärcher, B., Koch, D., Kinne, S., Kondo Y., Quinn, P.K., Sarofim, M.C., Schultz, M.G., Schulz, M., Venkataraman, C., Zhnag, H., Zhang, S., Bellouin, N., Guttikunda, S.K., Hopke, P.K., Jacobson, M.Z., Kaiser, J.W., Klimont, Z., Lohmann, U., Schwarz, J.P., Shindell, D., Storelvmo, T., Warren, S.G., Zender, C.S., 2013. Bounding the role of black carbon in the climate system: A scientific assessment. J. Geophys. Res. 118, 5380–5552.

Cappa, C.D., Onasch, T.B., Massoli, P., Worsnop, D.R., Bates, T.S., Cross, E.S., Davidovits, P., Hakala, J., Hayden, K.L., Jobson, B.T., Kolesar, K.R., Lack, D.A., Lerner, B.M., Li, S.-M., Mellon, D., Nuaaman, I., Olfert, J.S., Petäjä, T., Quinn, P.K., Song, C., Subramanian, R., Williams, E.J., Zaveri, R.A., 2012. Radiative absorption enhancements due to the mixing state of atmospheric black carbon. Science. 337, 1078–1081.

590 Cappa, C.D., Zhang, X., Russell, L.M., Collier, S., Lee, A.K.Y., Chen, C.-L., Betha, R., Chen, S.,
591 Liu, J., Price, D.J., Sanchez, K.J., McMeeking, G.R., Williams, L.R., Onasch, T.B., Worsnop,
592 D. R., Abbatt, J., Zhang, Q., 2019. Light absorption by ambient black and brown carbon
593 and its dependence on black carbon coating state for two California, USA, cities in
594 winter and summer. J. Geophys. Res. 2018JD029501.
595 Chan, T.W., Brook, J.R., Smallwood, G.J., Lu, G., 2011. Time-resolved measurements of
596 black carbon light absorption enhancement in urban and near-urban locations of
597 southern Ontario, Canada. Atmos. Chem. Phys. 11, 10407–10432.
598 Cheng, Y., He, K.B., Zheng, M., Duan, F.K., Du, Z.Y., Ma, Y.L., Tan, J.H., Yang, F.M., Liu, J.M.,
599 Zhang, X.L., 2011. Mass absorption efficiency of elemental carbon and water-soluble
600 organic carbon in Beijing, China, Atmos. Chem. Phys. 11, 11497–11510.
601 Cho, C., Kim, S.-W., Lee, M., Lim, S., Fang, W., Gustafsson, Ö., Andersson, A., Park, R.J., and
602 Sheridan, P.J., 2019. Observation-based estimates of the mass absorption cross-
603 section of black and brown carbon and their contribution to aerosol light absorption
604 in East Asia. Atmos. Environ., 212, 65–74.
605 Choi, J., Park, R.J., Lee, H.-M., Lee, S., Jo, D.S., Jeong, J.I., Henze, D.K., Woo, J.-H., Ban, S.-J.,
606 Lee, M.-D., Lim, C.-S., Park, M.-K., Shin, H.J., Cho, S., Peterson, D., Song, C.-K., 2019.
607 Impacts of local vs. trans-boundary emissions from different sectors on $PM_{2.5}$
608 exposure in South Korea during the KORUS-AQ campaign. Atmos. Environ. 203, 196–
609 205.
610 Choi, Y., Kanaya, Y., Park, S.-M., Matsuki, A., Sadanaga, Y., Kim, S.-W., Uno, I., Pan, X., Lee, M.,
611 Kim, H., and Jung, D. H., 2020. Regional variability in black carbon and carbon
612 monoxide ratio from long-term observations over East Asia: assessment of

613 representativeness for black carbon (BC) and carbon monoxide (CO) emission
614 inventories. Atmos. Chem. Phys. 20, 83–98.
615 Chung, C.E., Kim, S.-W., Lee, M., Yoon, S.-C., Lee, S., 2012a. Carbonaceous aerosol AÅE
616 inferred from in-situ aerosol measurements at the Gosan ABC super site, and the
617 implications for brown carbon aerosol. Atmos. Chem. Phys. 12, 6173–6184.
618 Chung, C.E., Ramanathan, V., Decremer, D., 2012b. Observationally constrained estimates
619 of carbonaceous aerosol radiative forcing. Proc. Natl. Acad. Sci. U. S. A. 109, 11624–
620 11629.
621 Cui, X., Wang, X., Yang, L., Chen, B., Chen, J., Andersson, A., Gustafsson, Ö., 2016. Radiative
622 absorption enhancement from coatings on black carbon aerosols. Sci. Total Environ.
623 551, 51–56.
624 DeCarlo, P.F., Kimmel, J.R., Trimborn, A., Northway, M.J., Jayne, J.T., Allison C.A., Gonin, M.,
625 Fuhrer, K., Horvath, T., Docherty, K.S., Worsnop, D.R., Jimenez, J.L., 2006. Field-
626 Deployable, High-Resolution, Time-of-Flight Aerosol Mass Spectrometer. Anal. Chem.
627 78, 8281–8289.
628 Gao, R. S., and Co-authors, 2007. A novel method for estimating light-scattering
629 properties of soot aerosols using a modified single-particle soot photometer, Aerosol
630 Sci. Technol. 41(2), 125–135.
631 Gustafsson, Ö., Ramanathan, V., 2016. Convergence on climate warming by black carbon
632 aerosols. Proc. Natl. Acad. Sci. U. S. A. 113, 4243–4245.
633 Gysel, M., Laborde, M., Olfert, J.S., Subramanian, R., Gröhn, A.J., 2011. Effective density of
634 Aquadag and fullerene soot black carbon reference materials used for SP2 calibration.
635 Atmos. Meas. Tech. Discuss. 4, 4937–4955.

636 Healy, R.M., Wang, J.M., Jeong, C.-H., Lee, A.K.Y., Willis, M.D., Jaroudi, E., Zimmerman, N.,
637 Hilker, N., Murphy, M., Eckhardt, S., Stohl, A., Abbatt, J.P.D., Wenger, J.C., Evans, G.J.,
638 2015. Light-absorbing properties of ambient black carbon and brown carbon from
639 fossil fuel and biomass burning sources. J. Geophys. Res. 120, 6619–6633.
640 Hess, M., Koepke, P., Schult, I., 1998. Optical Properties of Aerosols and Clouds: The
641 Software Package OPAC. Bull. Amer. Meteor. Soc. 79, 831–844.
642 Jacobson, M.Z., 2001. Strong radiative heating due to the mixing state of black carbon in
643 atmospheric aerosols, Nature, 409, 695–697.
644 Jacobson, M.Z., 2013. Radiative absorption enhancement due to the mixing state of
645 atmospheric black carbon, Science, 339, 393.
646 Jimenez, J.L., and Co-authors, 2003. Evolution of organic aerosols in the atmosphere,
647 Science, 326, 1525–1529.
648 Jordan, Carolyn E., James H. Crawford, Andreas J. Beyersdorf, Thomas F. Eck, Hannah S.
649 Halliday, Benjamin A. Nault, Lim-Seok Chang, and Co-authors, 2020. Investigation of
650 factors controlling PM2.5 variability across the South Korean Peninsula during
651 KORUS-AQ, Elementa: Science of the Anthropocene, 8.
652 Kanaya, Y., Pan, X., Miyakawa, T., Komazaki, Y., Taketani, F., Uno, I., Kondo, Y., 2016. Long-
653 term observations of black carbon mass concentrations at Fukue Island, western
654 Japan, during 2009–2015: constraining wet removal rates and emission strengths
655 from East Asia. Atmos. Chem. Phys. 16, 10689–10705.
656 Kim, H., Zhang, Q., Heo, J., 2018. Influence of intense secondary aerosol formation and
657 long-range transport on aerosol chemistry and properties in the Seoul Metropolitan
658 Area during spring time: results from KORUS-AQ. Atmos. Chem. Phys. 18, 7149–7168.

659 Klawonn, I., Bonaglia, S., Whitehouse, M.J., Littmann, S., Tienken, D., Kuypers, M.M.M.,
660 Brüchert, V., Ploug, H., 2019. Untangling hidden nutrient dynamics: rapid ammonium
661 cycling and single-cell ammonium assimilation in marine plankton communities.
662 ISME J., 13, 1960–1974.
663 Kondo, Y., Sahu, L., Kuwata, M., Miyazaki, Y., Takegawa, N., Moteki, N., Imaru, J., Han, S.,
664 Nakayama, T., Oanh, N.T.Kim., Hu, M., Kim, Y.J., Kita, K., 2009. Stabilization of the mass
665 absorption cross section of black carbon for filter-based absorption photometry by
666 the use of a heated inlet. Aerosol Sci. Technol. 43, 741–756.
667 Kondo, Y., Matsui, H., Moteki, N., Sahu, L., Takegawa, N., Kajino, M., Zhao, Y., Cubison, M.J.,
668 Jimenez, J.L., Vay, S., Diskin, G.S., Anderson, B., Wisthaler, A., Mikoviny, T., Fuelberg,
669 H.E., Blake, D.R., Huey, G., Weinheimer, A.J., Knapp, D.J., Brune, W.H., 2011. Emissions
670 of black carbon, organic, and inorganic aerosolsfrom biomass burning in North
671 America and Asia in 2008. J. Geophys. Res. 116, D08204.
672 Lamb, K.D., and Co-authors., 2018. Estimating Source Region Influences on Black Carbon
673 Abundance, Microphysics, and Radiative Effect Observed Over South Korea. J.
674 Geophys. Res. 123, 527–548.
675 Leung, K.K., Schnitzler, E.G., Jäger, W., Olfert, J.S., 2017. Relative humidity dependence of
676 soot aggregate restructuring induced by secondary organic aerosol: Effects of water
677 on coating viscosity and surface tension. Environ. Sci. Technol. Lett. 4, 386–390.
678 Lim, S., Lee, M., Kim, S.-W., Laj, P., 2018. Sulfate alters aerosol absorption properties in
679 East Asian outflow. Sci. Rep. 8, 5172.
680 Liu, S., Aiken, A.C., Gorkowski, K., Dubey, M.K., Cappa, C.D., Williams, L.R., Herndon, S.C.,
681 Massoli, P., Fortner, E.C., Chhabra, P.S., Brooks, W.A., Onasch, T.B., Jayne, J.T., Worsnop,
682 D.R., China, S., Sharma, N., Mazzoleni, C., Xu, L., Ng, N.L., Liu, D., Allan, J.D., Lee, J.D.,

683 Fleming, Z. L., Mohr, C., Zotter, P., Szidat, S., Prévôt, A.S.H., 2015. Enhanced light
684 absorption by mixed source black and brown carbon particles in UK winter. Nat.
685 Commun. 6, 8435.
686 Liu, H., Pan, X., Liu, D., Liu, X., Chen, X., Tian, Y., Sun, Y., Fu, P., Wang, Z., 2020. Mixing
687 characteristics of refractory black carbon aerosols at an urban site in Beijing. Atmos.
688 Chem. Phys. 20, 5771–5785.
689 Ma, Y., Huang, C., Jabbour, H., Zheng, Z., Wang, Y., Jiang, Y., Zhu, W., Ge, X., Collier, S., Zheng,
690 J., 2020. Mixing state and light absorption enhancement of black carbon aerosols in
691 summertime Nanjing, China. Atmos. Environ. 222, 117141.
692 Magi, B. I., Hobbs, P. V., Schmid, B., Redemann, J., 2003. Vertical profiles of light scattering,
693 light absorption, and single scattering albedo during the dry, biomass burning season
694 in southern Africa and comparisons of in situ and remote sensing measurements of
695 aerosol optical depths. J. Geophys. Res. 108, D13, 8504.
696 McMeeking, G.R., Hamburger, T., Liu, D., Flynn. M., Morgan, W.T., Northway, M., Highwood,
697 E.J., Krejci, R., Allan, J.D., Minikin, A., Coe, H., 2010. Black carbon measurements in the
698 boundary layer over western and northern Europe. Atmos. Chem. Phys. 10, 9393–
699 9414.
700 McMeeking, G.R., Good, N., Petters, M.D., McFiggans, G., Coe, H., 2011. Influences on the
701 fraction of hydrophobic and hydrophilic black carbon in the atmosphere. Atmos.
702 Chem. Phys. 11, 5099–5112.
703 McMeeking, G.R., Fortner, E., Onasch, T.B., Taylor. J.W., Flynn, M., Coe, H., Kreidenweis, S.M.
704 2014. Impacts of nonrefractory material on light absorption by aerosols emitted from
705 biomass burning. J. Geophys. Res. 119, 272–286.

Moteki, N., Kondo, Y., 2010. Dependence of Laser-Induced Incandescence on Physical Properties of Black Carbon Aerosols: Measurements and Theoretical Interpretation. Aerosol Sci. Tech. 44, 663–675.

Moteki, N., Kondo, Y., Oshima, N., Takegawa, N., Koike, M., Kita, K., 2012. Size dependence of wet removal of black carbon aerosols during transport from the boundary layer to the free troposphere. Geophys. Res. Lett., 39, L13802.

Nakayama, T., Ikeda, Y., Sawada, Y., Setoguchi, Y., Ogawa, S., Kawana, K., Mochida, M., Ikemori, F., Matsumoto, K., Matsumi, Y., 2014. Properties of light-absorbing aerosols in the Nagoya urban area, Japan, in August 2011 and January 2012: Contributions of brown carbon and lensing effect. J. Geophys. Res. 119, 721–739.

Nault, B.A., and Co-authors, 2018. Secondary organic aerosol production from local emissions dominates the organic aerosol budget over Seoul, South Korea, during KORUS-AQ. Atmos. Chem. Phys. 18, 17769–17800.

NIER and NASA, 2017. KORUS-AQ Rapid Science Synthesis Report. Available at https://espo.nasa.gov/korus-aq/content/KORUS-AQ_White_Paper.

Oak, Y.j., Park, R.J., Schroeder, J.R., Crawford, J.H., Blake, D.R., Weinheimer, A.J., Woo, J.-H., Kim, S.-W., Yeo, H., Fried, A., Wisthaler, A., Brune, W.H., 2019. Evaluation of simulated O3 production efficiency during the KORUS-AQ campaign: Implications for anthropogenic NO_x emissions in Korea, Elem. Sci. Anth. 7, 56.

Ohata, S., Moteki, N., Mori, T., Koike, M., Kondo, Y., 2016. A key process controlling the wet removal of aerosols: New observational evidence. Sci. Rep. 6, 34113.

Ohsima, N., Koike, M., Zhang, Y., Kondo, Y., Moteki, N., Takegawa, N., Miyazaki, Y., 2009. Aging of black carbon in outflow from anthropogenic sources using a mixing state resolved model: Model development and evaluation. J. Geophys. Res. 114, D06210.

730 Park, M. Yum, S.S., Kim, N., Anderson, B.E., Beyersdorf, A., Thornhill, K.L., 2020. On the
731 submicron aerosol distributions and CCN activity in and around the Korean Peninsula
732 measured onboard the NASA DC-8 research aircraft during the KORUS-AQ field
733 campaign. Atmos. Res. 243, 105004.
734 Peng, J., Hu, M., Guo, S., Du, Z., Zheng, J., Shang, D., Zamora, M.L., Zeng, L., Shao, M., Wu,
735 Y.S., Zheng, J., Wang, Y., Glen, C.R., Collins, D.R., Molina, M.J., Zhang, R., 2016. Markedly
736 enhanced absorption and direct radiative forcing of black carbon under polluted
737 urban environments. Proc. Natl. Acad. Sci. U. S. A. 113, 4266–4271.
738 Peterson, D.A., Hyer, E.J., Han, S.O., Crawford, J.H., Park, R.J., Holz, R., Kuehn, R.E., Eloranta,
739 E., Knote, C., Jordan, C.E. and Lefer, B.L., 2019. Meteorology influencing springtime air
740 quality, pollution transport, and visibility in Korea. Elementa: Science of the
741 Anthropocene, 7.
742 Popovicheva, O.B., Persiantseva, N.M., Kireeva, E.D., Khokhlova, T.D., Shonija, N.K., 2011.
743 Quantification of the hygroscopic effect of soot aging in the atmosphere: Laboratory
744 simulations. J. Phys. Chem. 115, 298–306.
745 Ram, K., Sarin, M.M., 2009. Absorption coefficient and site-specific mass absorption
746 efficiency of elemental carbon in aerosols over urban, rural, and high-altitude sites in
747 India. Environ. Sci. Technol. 43, 8233–8239.
748 Ramana, M.V., Ramanathan, V., Feng, Y., Yoon, S.-C., Kim, S.-W., Carmichael, G.R., Schauer,
749 J.J., 2010. Warming influenced by the ratio of sulphate and the black-carbon source.
750 Nat. Geosci. 3, 542–545.
751 Redemann, J., and Co-authors, 2000. Retrieving the vertical structure of the effective
752 aerosol complex index of refraction from a combination of aerosol in situ and remote
753 sensing measurements during TARFOX, J. Geophys. Res. 105, 9949–9970.

754 Schwarz, J.P., and Co-authors., 2006. Single-particle measurements of midlatitude black
755 carbon and light-scattering aerosols from the boundary layer to the lower
756 stratosphere, J. Geophys. Res. 111, D16207.
757 Schwarz, J.P., and Co-authors., 2008. Measurement of the mixing state, mass, and optical
758 size of individual black carbon particles in urban and biomass burning emissions,
759 Geophys. Res. Lett. 35, L13810.
760 Schwarz, J.P., Samset, B.H., Perring, A.E., Spackman, J.R., Gao, R.S., Stier, P., Schulz, M.,
761 Moore, F.L., Ray. E.A., Fahey, D.W., 2013. Global-scale seasonally resolved black carbon
762 vertical profiles over the Pacific, Geophys. Res. Lett., 40, 5542–5547.
763 Sedlacek, A.J., Lewis, E.R., Kleinman, L., Xu, J., Zhang, Q., 2012. Determination of and
764 evidence for non-core-shell structure of particles containing black carbon using the
765 single-particle soot photometer (SP2), Geophys. Res. Lett., 39, L06802.
766 Shiraiwa, M., Kondo, Y., Moteki, N., Takegawa, M., Miyazaki, Y., Blake, D.R., 2007. Evolution
767 of mixing state of black carbon in polluted air from Tokyo. Geophys. Res. Lett. 34,
768 L16803.
769 Shiraiwa, M., Kondo, Y., Iwamoto, T., Kita, K., 2010. Amplification of Light Absorption of
770 Black Carbon by Organic Coating. Aerosol Sci. Tech. 44, 46–54.
771 Si, Y., Li, S., Chen, L., Yu, C., Zhu, W., 2017. Estimation of Satellite-Based SO42− and NH4+
772 Composition of Ambient Fine Particulate Matter over China Using Chemical Transport
773 Model. Remote Sens. 9, 817.
774 Spackman, J.R., Schwarz, J.P., Gao, R.S., Watts, L.A., Thomson, D.S., Fahey, D.W., Holloway,
775 J.S., Gouw, J.A., Trainer, M., Ryerson, T.B., 2008. Empirical correlations between black
776 carbon aerosol and carbon monoxide in the lower and middle troposphere. Geophys.
777 Res. Lett. 35, L19816.

778 Taylor, J.W., Allan, J.D, Allen, G., Coe, H., Williams, P.I., Flynn, M.J., Le Breton, M., Muller,
779 J.B.A., Percival, C.J., Oram, D., Forster, G., Lee, J.D., Rickard, A.R., Parrington, M., Palmer,
780 P.I., 2014. Size-dependent wet removal of black carbon in Canadian biomass burning
781 plumes. Atmos. Chem. Phys. 14, 13755–13771.
782 Toon, O.B., Ackerman, T.P., 1981. Algorithms for the calculation of scattering by stratified
783 spheres. Appl. Opt. 20. 3657–3660.
784 Wang, X., Heald, C.L., Ridley, D.A., Schwarz, J.P., Spackman, J.R., Perring, A.E., Coe, H., Liu,
785 D., Clarke, A.D., 2014. Exploiting simultaneous observational constraints on mass and
786 absorption to estimate the global direct radiative forcing of black carbon and brown
787 carbon. Atmos. Chem. Phys. 14, 10989–11010.
788 Wenzel, M., Gorzawski, H., Naumann, K.-H., Saathoff, H., Weinbruch, S., 2003.
789 Transmission electron microscopical and aerosol dynamical characterization of soot
790 aerosol. J. Aerosol Sci. 34, 1445–1463.
791 Wofsy, S.C., and Co-authors, 2011. HIAPER Pole-to-Pole observations (HIPPO): Fine-
792 grained, global-scale measurements of climatically important atmospheric gases and
793 aerosols, Philos. Trans. R. Soc. A-Math. Phys. Eng. Sci., 369, 2073–2086.
794 Wu, C., Wu, D., Yu, J.Z., 2018. Quantifying black carbon light absorption enhancement
795 with a novel statistical approach. Atmos. Chem. Phys. 18, 289–309.
796 Xie, C., Xu, W., Wang, J., Liu, D., Ge, X., Zhang, Q., Wang, Q., Du, W., Zhao, J., Zhou, W., Li, J.,
797 Fu, P., Wang, Z., Worsnop, D., Sun, Y., 2019. Light absorption enhancement of black
798 carbon in urban Beijing in summer. Atmos. Environ. 2019, 499–504.
799 Yang, M., Howell, S.G., Zhuang, J., Huebert, B.J., 2009. Attribution of aerosol light
800 absorption to black carbon, brown carbon, and dust in China–interpretations of
801 atmospheric measurements during EAST-AIRE. Atmos. Chem. Phys. 9, 2035–2050.

802 Zhang, X., Mao, M., Yin, Y., Wang, B., 2017. Absorption enhancement of aged black carbon
803 aerosols affected by their microphysics: A numerical investigation. J. Quant. Spectrosc.
804 Radiat. Transf. 202, 90–97.
805 Zhang, Y., Zhang, Q., Cheng, Y., Su, H., Kecorius, S., Wang, Z., Wu, Z., Hu, M., Zhu, T.,
806 Wiedensohler, A., He, K., 2016. Measuring the morphology and density of internally
807 mixed black carbon with SP2 and VTDMA: New insight into the absorption
808 enhancement of black carbon in the atmosphere. Atmos. Meas. Tech. 9, 1833–1843.
809 Zhang, Y., Forrister, H., Liu, J., Dibb, J., Anderson, B., Schwarz, J.P., Perring, A.E., Jimenez,
810 J.L., Campuzano-Jost, P., Wang, Y., Nenes, A., Weber Rodney J., 2017. Top-of-
811 atmosphere radiative forcing affected by brown carbon in the upper troposphere. Nat.
812 Geosci. 10, 486–491.
813 Zhang, Y., and Co-authors, 2018a. Effect of the Aerosol-Phase State on Secondary Organic
814 Aerosol Formation from the Reactive Uptake of Isoprene-Derived Epoxydiols (IEPOX).
815 Environ. Sci. Technol. Lett. 5, 167–174.
816 Zhang, Y., and Co-authors, 2018b. Evidence of major secondary organic aerosol
817 contribution to lensing effect black carbon absorption enhancement. Npj Climate and
818 Atmospheric Science. 47, 1–8.
819 Zhang, Q., and Co-authors, 2008. Asian emission in 2006 for the NASA INTEX-B mission.
820 Atmos. Chem. Phys. 9, 5131–5153.
821

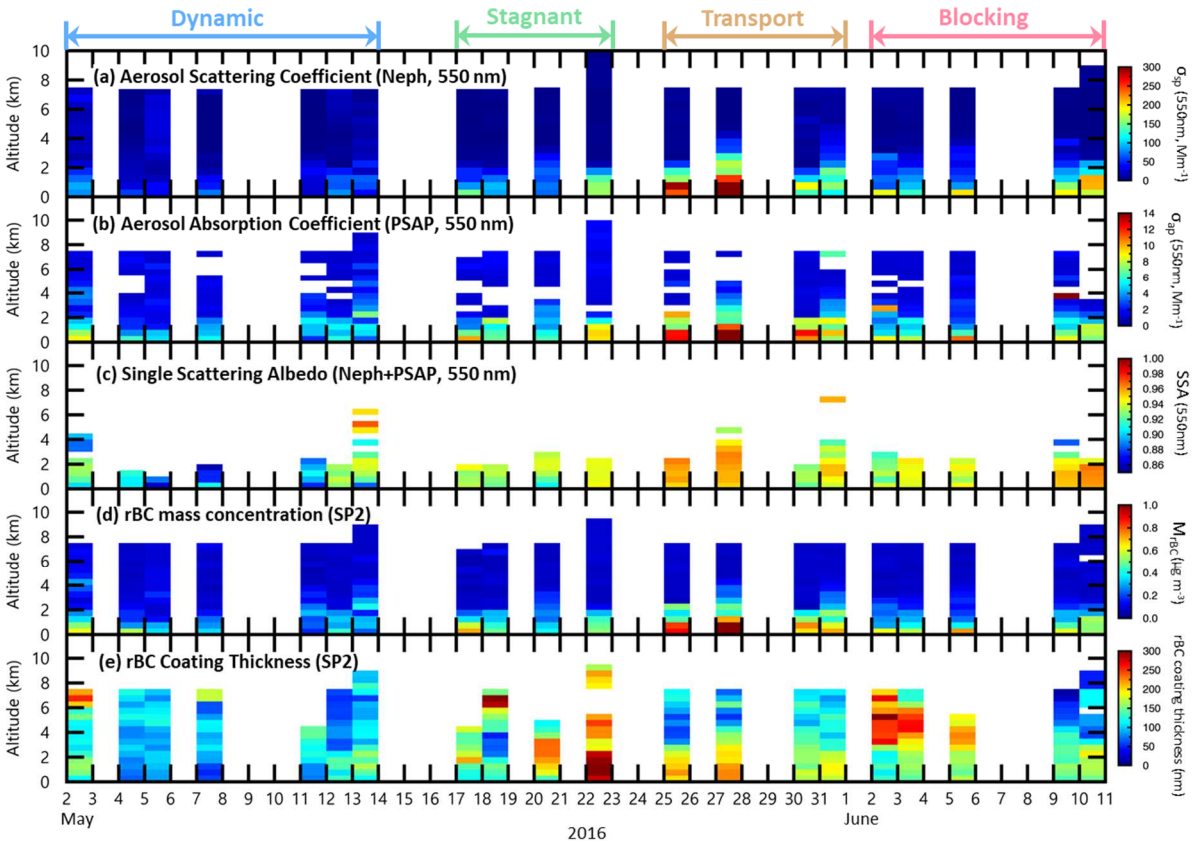

Figure 1. Overview of temporal variations in aerosol optical properties and refractory black carbon (rBC) physical properties: (a) aerosol scattering coefficient, (b) aerosol absorption coefficient, (c) single scattering albedo, (d) rBC mass concentration, and (e) rBC coating thickness from aircraft observation during the KORUS-AQ campaign.

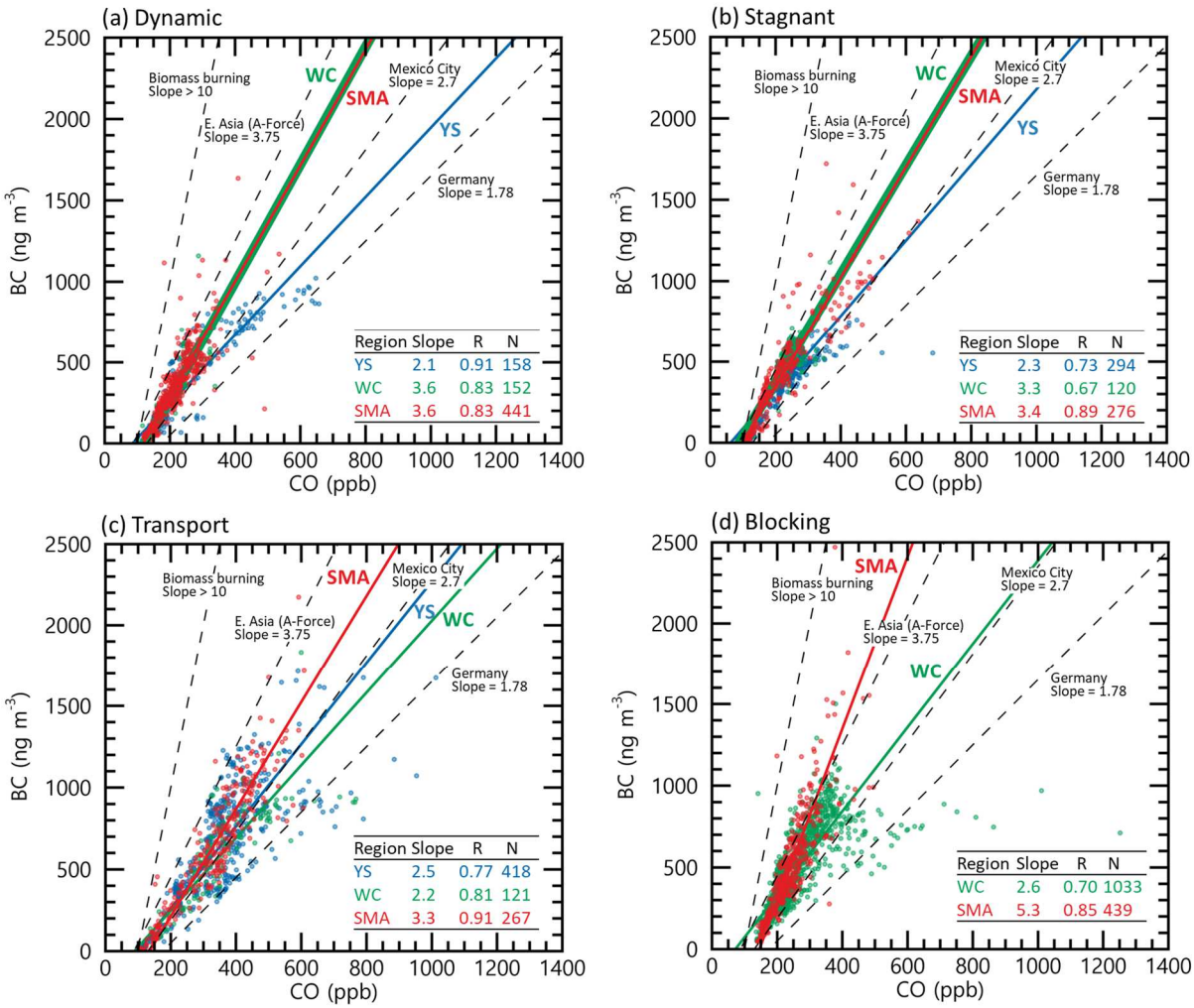

Figure 2. BC/CO ratios in the Yellow Sea (YS), West Coast (WC), and Seoul Metropolitan Area (SMA) in the (a) dynamic, (b) stagnant, (c) transport, and (d) blocking periods during the KORUS-AQ campaign. BC/CO slopes reported in previous studies are represented with black dashed lines.

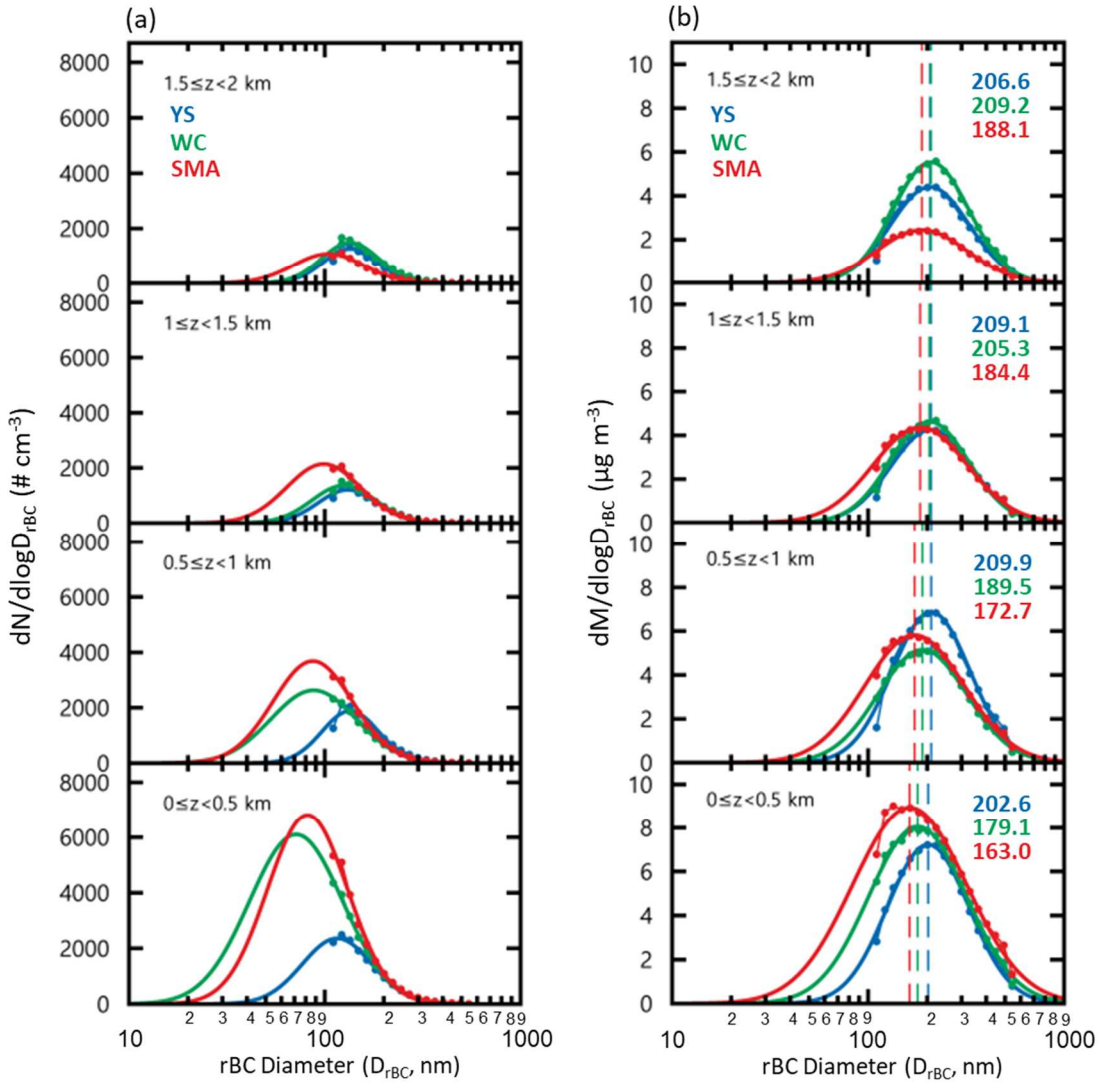

834

835 **Figure 3**. Size distributions of rBC particles. (a) Number size distributions, and (b) mass
836 size distributions in the Yellow Sea (blue), West Coast (green), and Seoul (red) during
837 the KORUS-AQ campaign. The size distributions were divided into four layers (0≤z<0.5
838 km, 0.5≤z<1.0 km, 1.0≤z<1.5 km, 1.5≤z<2 km), and the dashed-lines and values
839 represent the mass median diameter (MMD).

840

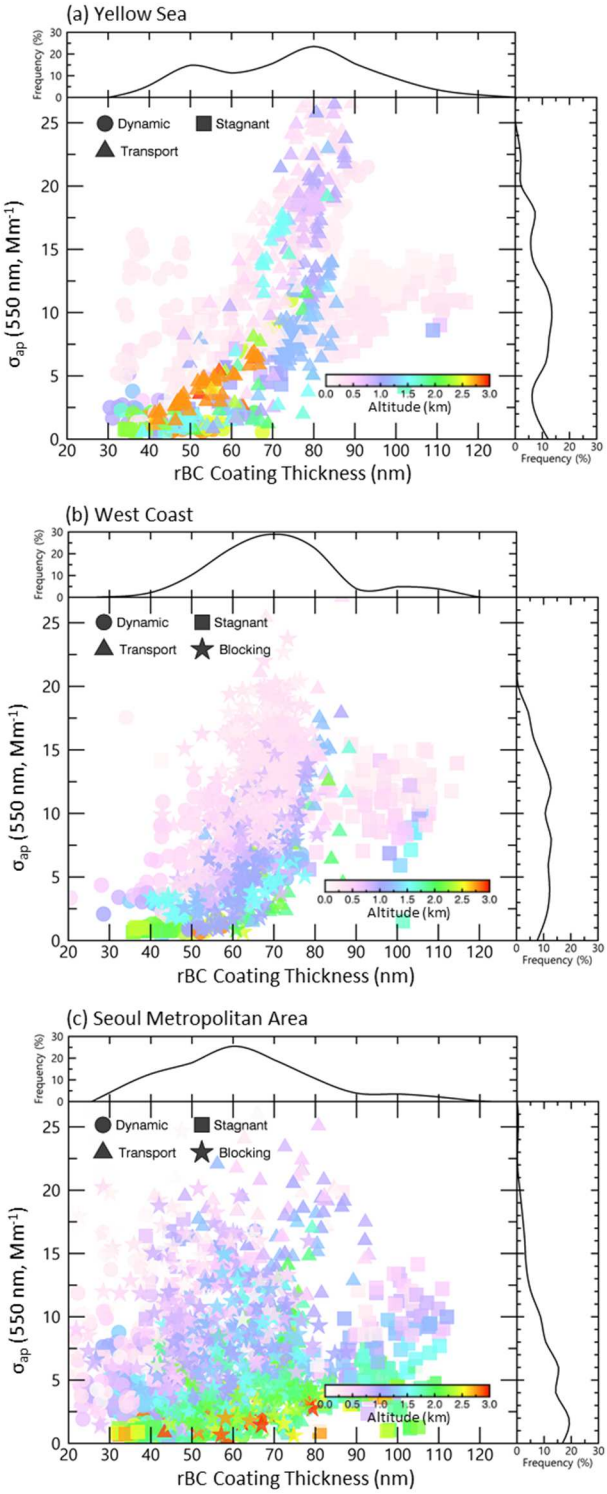

841

842 **Figure 4**. Relationships of rBC coating thickness and aerosol absorption coefficient (σ_{ap})
843 from PSAP at 550 nm in the (a) Yellow Sea, (b) West Coast, and (c) Seoul Metropolitan
844 Area during the KORUS-AQ campaign. The colors represent observed altitudes. The
845 symbols represent observed period (circle: dynamic, square: stagnant, triangle:
846 transport, star: blocking). The frequency of rBC coating thickness and σ_{ap} are
847 represented at the top and right of the figure, respectively.

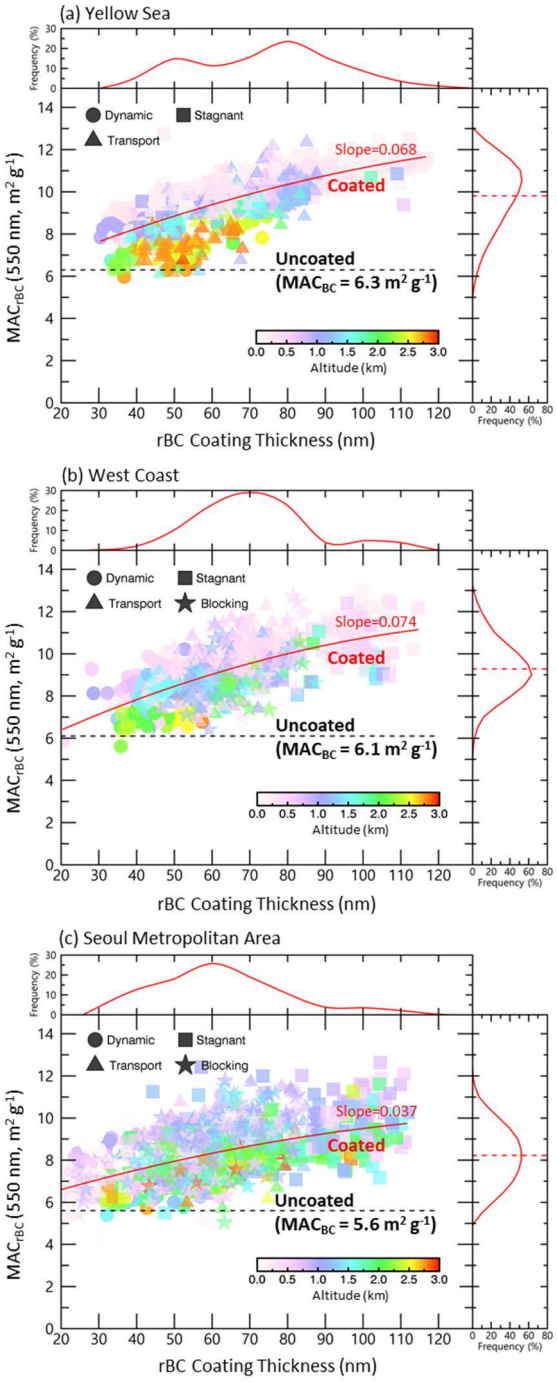

Figure 5. Relationships of rBC coating thickness and mass absorption cross-section (MAC) of coated rBC at 550 nm in the (a) Yellow Sea, (b) West Coast, and (c) Seoul Metropolitan Area during the KORUS-AQ campaign. The dashed black lines represent averaged MAC of uncoated rBC, and colored symbols represent MAC of coated rBC (MAC_{rBC}^{Coated}). The colors represent observed altitudes. The symbols represent observed period (circle: dynamic, square: stagnant, triangle: transport, star: blocking). The frequency of rBC coating thickness and MAC_{rBC}^{Coated} are represented at the top and right of the figure, respectively.

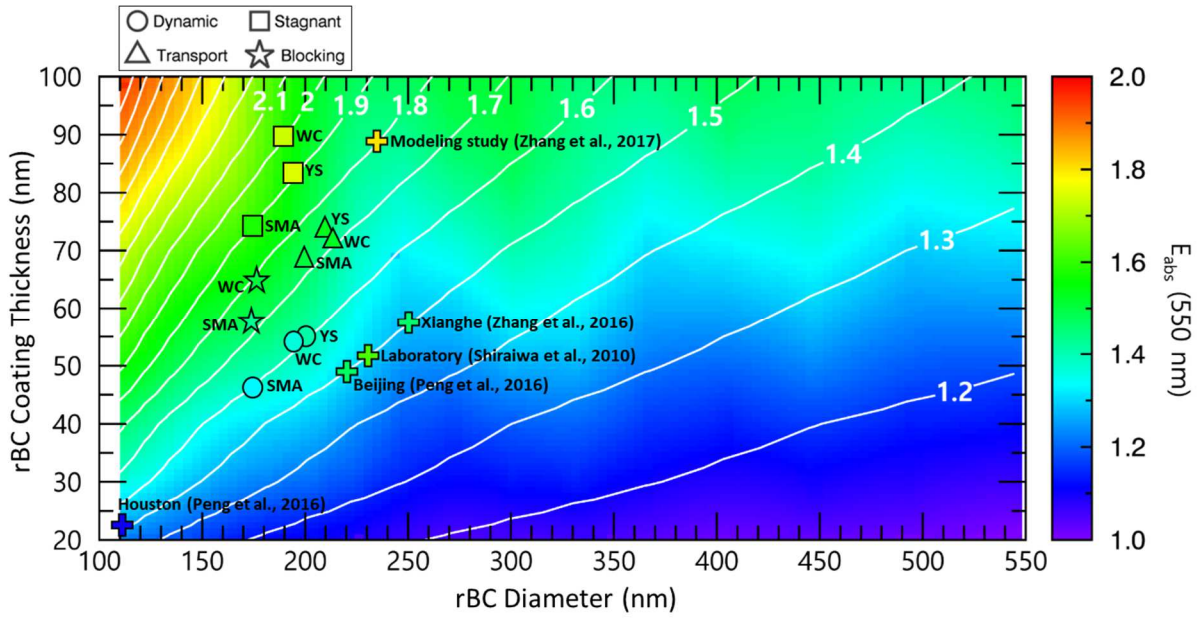

857

858 **Figure 6**. Enhancement of BC absorption (E_{abs}) at 550 nm as functions of rBC diameter
859 and coating thickness during the KORUS-AQ campaign. White lines represent the ratios
860 between the coated and uncoated rBC radius. Average value in three regions and four
861 periods in this study and values in previous studies are displayed in the figure.

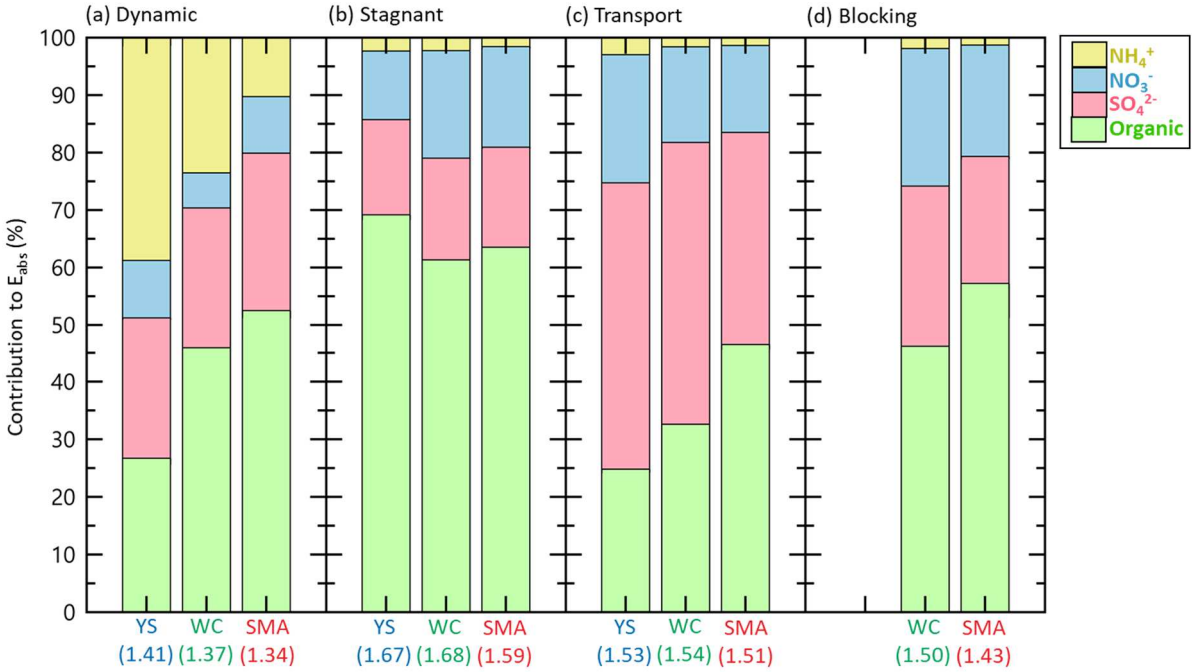

Figure 7. Contribution of chemical composition (green: organic, red: SO_4^{2-}, blue: NO_3^-, and yellow: NH_4^+) to Eabs at the Yellow Sea (YS), West Coast (WC), and Seoul Metropolitan Area (SMA) during (a) dynamic, (b) stagnant, (c) transport, and (d) blocking period. The values in parenthesis represent average E_{abs}.

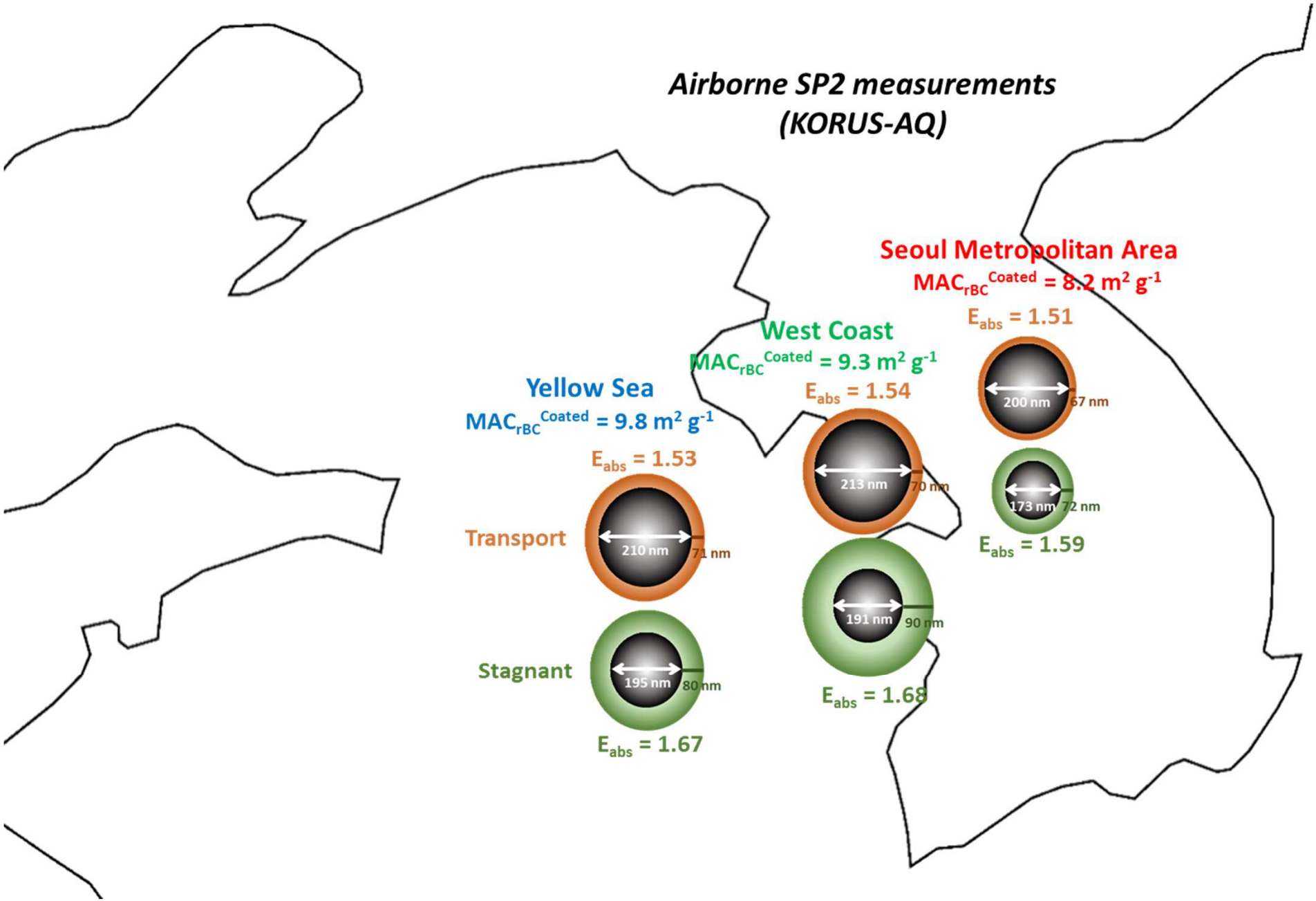
Airborne SP2 measurements
(KORUS-AQ)
Seoul Metropolitan Area
MAC_rBC^Coated = 8.2 m² g⁻¹
E_abs = 1.51
200 nm
67 nm
West Coast
MAC_rBC^Coated = 9.3 m² g⁻¹
E_abs = 1.54
213 nm
70 nm
173 nm
72 nm
E_abs = 1.59
Yellow Sea
MAC_rBC^Coated = 9.8 m² g⁻¹
E_abs = 1.53
Transport
210 nm
71 nm
191 nm
90 nm
E_abs = 1.68
Stagnant
195 nm
80 nm
E_abs = 1.67